Gorbachev *et al.*
Protection and Control of Modern Power Systems (2023) 8:52
https://doi.org/10.1186/s41601-023-00325-7

Protection and Control of
Modern Power Systems

ORIGINAL RESEARCH Open Access

MPC-based LFC for interconnected power systems with PVA and ESS under model uncertainty and communication delay

Sergey Gorbachev[1], Jinrui Guo[2,3], Ashish Mani[1*], Li Li[1], Long Li[4], Chunxia Dou[2*], Dong Yue[2,3] and Zhijun Zhang[2,3]

Abstract
In this paper, a cloud-edge-end collaboration-based control architecture is established for frequency regulation in interconnected power systems (IPS). A model predictive control (MPC)-based load frequency control strategy for the IPS with photovoltaic aggregation and energy storage systems under model uncertainty and communication delay is proposed. This can effectively overcome the issues of model uncertainty, random load perturbation and communication delay. First, a state space model for the IPS is constructed. To coordinate the frequency and contact line power fluctuation of the IPS, a robust controller based on the theory of MPC is then designed. Then, considering the communication delay of frequency response commands during transmission, a predictive compensation mechanism is introduced to eliminate the effect of delay while considering model uncertainty. Finally, simulation results verify the effectiveness and robustness of the proposed control strategy.

Keyword Cloud-edge-end collaboration interconnected power systems load frequency control photovoltaics aggregation model predictive control predictive compensation mechanism

1 Introduction

Maintaining frequency stability is critical to the safe operation of power systems [1]. To improve the reliability of power systems, multiple independent generation areas are interconnected via contact lines to form interconnected power systems (IPS) [2]. Automatic generation control is the key to maintaining the stable operation of IPS, while load frequency control (LFC) is one of important components [3]. LFC reduces the frequency deviation and contact line power fluctuation of the IPS. In addition, an increasing number of decentralized renewable energy sources (RESs) are being connected to the power grid because of the increasing environmental challenges arising from conventional power sources [4]. RESs' randomness and volatility may increase oscillations and cause system instability and blackout accidents [5, 6]. Nevertheless, in order to avoid frequency deviation and contact line power fluctuation caused by RESs to the IPS, it is usually necessary to use information and communication technology to control the aggregation of massive decentralized distributed RESs such as photovoltaics and energy storage systems (ESS) [7, 8].

Considering photovoltaic aggregation (PVA) and ESS (such as capacitive energy storage [9]) access to the IPS, employing an efficient LFC controller can effectively

*Correspondence:
Ashish Mani
mani.ashish@gmail.com
Chunxia Dou
cxdou@ysu.edu.cn
[1] School of Artificial Intelligence, Chongqing University of Education, Chongqing 400065, China
[2] Institute of Advanced Technology for Carbon Neutral, Nanjing University of Posts and Telecommunications, Nanjing 210023, China
[3] College of Automation and College of Artificial Intelligence, Nanjing University of Posts and Telecommunications, Nanjing 210023, China
[4] School of Mathematics and Big Data, Chongqing University of Education, Chongqing 400065, China

enhance the stability of the system frequency. To guarantee safe and efficient power supply of the IPS, the LFC needs to have good resistance to load perturbation and robustness against system model uncertainty [6]. Thus, in addition to accessing PVA and ESS units, it is essential and imperative to design an advanced and robust LFC strategy to reduce frequency deviation and contact line power fluctuation of the IPS.

1.1 Literature review

Over the past few decades, there have been a lot of studies on LFC. Classical proportional integral (PI) control was first adopted to solve the LFC problem [10]. However, issues such as system uncertainty, load variation and external disturbance occur in power system operation [11], all of which affect the performance of traditional PI control. In view of these limitations, many researchers employed the method of optimizing PI controller parameters to address the frequency control issue and improve the stability of the system, including: (1) based on physical optimization algorithms, such as simulated annealing (SA) [12], gravitational search algorithm (GSA) [13], etc.; (2) based on group optimization algorithms, such as the artificial bee colony algorithm (ABC) [14], cuckoo search (CS) [15], etc.; and (3) based on evolutionary optimization algorithms, such as the genetic [16] and firefly algorithms [17], etc. For modern power systems, there exist multiple constraint situations. Consequently, the above optimization algorithms encounter the issue of long processing time owing to slow convergence and dimensional catastrophe [18]. These render them arduous in accomplishing the expected control effect for classical PI control.

Hence, there have been numerous studies on LFC controllers based on modern control theory. Reference [19] proposes robust control to address the LFC problem of multi-region IPS due to load perturbation and parameter uncertainty. For the LFC problem of multi-source and multi-area IPS, a variable structure control method is introduced in [20], while in order to maintain the stable operation of IPS, reference [21] designs a fuzzy logic controller. In [22], a neural network approach is applied to the LFC controller to reduce the frequency fluctuation of IPS caused by load perturbation. In order to guarantee that the frequency fluctuation of multi-area IPS can converge to a small range, reference [23] designs an adaptive control strategy. The modern control methods mentioned above can indeed tackle issues such as system uncertainty to enhance performance of IPS, but they also affect the control effects because of factors such as inaccurate models and complex actual system structures, and there are defects in practical application [24]. The Flexible AC transmission system (FACTS) is employed for an LFC to improve the quality of power supply in [25], whereas in [26], a sliding mode control method is proposed for the problem of IPS frequency fluctuation caused by random load change and system parameter uncertainty. However, so far, there exist few studies on the LFC of PVA and ESS access to the IPS under the conjunction of model uncertainty and intra-area communication delay.

The controller based on model predictive control (MPC) has strong ability to deal with system uncertainties and external disturbances [24]. Thus it has been widely used in power systems, such as frequency control [24, 27], optimal scheduling [28, 29] and voltage control [30, 31]. MPC can predict the future system state according to the state space model of the system, compare with the control reference signal in each sampling period, and perform rolling optimization to the output optimal control signals of the system combining with the system constraints [32]. Consequently, based on MPC, this paper combines the cloud-edge-end collaboration-based LFC architecture, and proposes a predictive compensation mechanism (PCM) strategy to design the LFC controller to enhance the dynamic performance of the IPS with PVA and ESS under model uncertainty and communication delay. To the extent of the authors' knowledge, this is the first time that the cloud-edge-end collaboration-based LFC architecture is designed based on the cloud-edge collaboration information architecture [33].

1.2 Contributions

The main contributions of this work are:

(1) A cloud-edge-end collaboration-based LFC architecture is proposed to support the safe and stable operation of the IPS based on the cloud-edge collaboration information architecture. It is dedicated to facilitating the participation of multi-regional power systems in frequency regulation by providing a unified cloud control center. Thus, the frequency issues of the IPS may be solved over a large area and wide scale via the collaborative work of edge servers.

(2) Compared with the work in [24, 34], the proposed IPS model fully considers the positive effect of the PVA and ESS on system frequency control. The model can effectively mitigate the frequency and contact line power deviations, and guarantee the safe and efficient power supply of the IPS. Therefore, it may be a new design reference for the studied IPS.

(3) Based on the proposed IPS model, a state space model considering PVA and ESS access to the IPS is first established. Compared with [24, 27], this paper designs an MPC-based controller based on

the proposed state space model, and considers the influence of model uncertainty and communication delay. This improves the robustness and security of the IPS.

(4) In different case scenarios, compared with traditional PI control [10, 35], the superiority of the proposed strategy in frequency regulation and the effectiveness of the PCM in eliminating the influence of time delay are validated.

To make the proposed control strategy easier to comprehend, a diagrammatic overview of the entire paper is presented in Fig. 1.

1.3 Paper organization

The rest of this paper is summarized as follows: in Sect. 2, the IPS frequency control architecture and model are presented, while Sect. 3 describes the design of the MPC-based controller and PCM considering model uncertainty. Simulation results are provided in Sect. 4 to verify the superiority of the proposed control strategy, and Sect. 5 concludes the paper.

2 System description and modeling

In this section, a cloud-edge-end collaboration-based LFC architecture for the IPS is proposed. The mathematical model of each component of the studied IPS is presented separately, and then the state space model of the IPS is deduced.

2.1 Frequency control architecture of IPS

The cloud-edge-end collaboration-based LFC architecture is depicted in Fig. 2, where the cloud-edge-end layers form

the computation, communication and control parts of the IPS. The end layer is responsible for collecting real-time operational status information of the system devices and receiving frequency control commands from the cloud layer. The edge servers at the edge layer provide the ability to extract the state information of the underlying system devices into multiple logical entities at the cloud layer and interact with the control center via communication links and power connections [30, 36]. The control center at the cloud layer deploys computation and decision-making functions. When

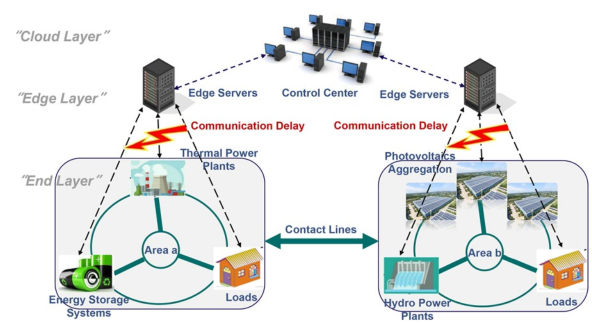

Fig. 2 Description of the cloud-edge-end collaboration based control architecture

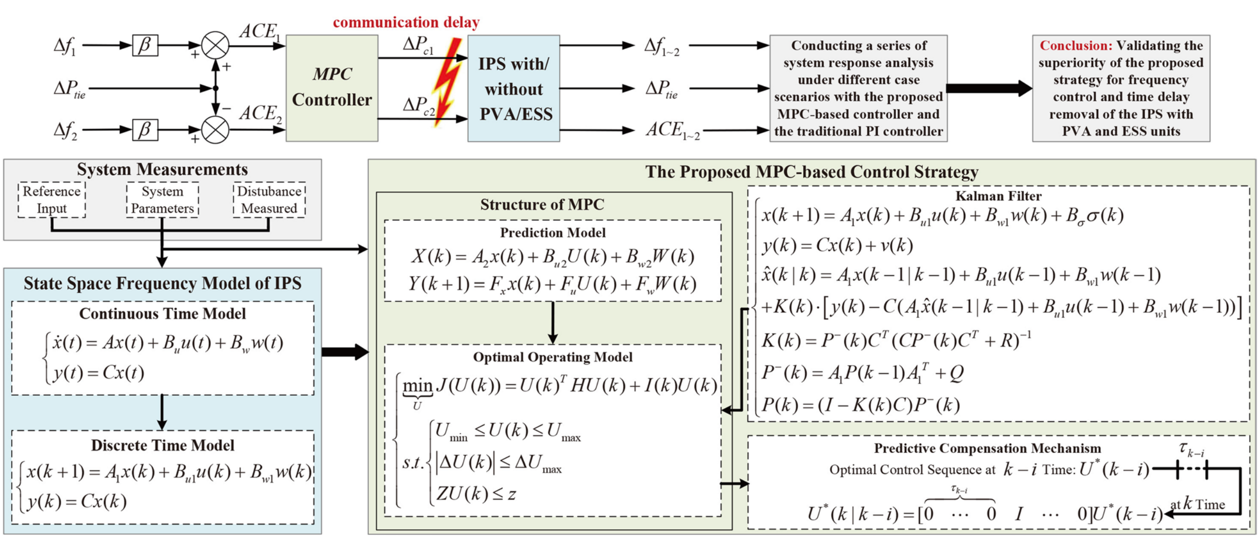

Fig. 1 Diagram overview of the proposed work

the system suffers from a frequency fluctuation that exceeds the safety margin, the control center sends frequency response commands to each control device at the end layer.

Remark 1 Note that this paper only considers the case where the time delay occurs on the downlink communication channel between the edge layer and the end layer in the frequency control architecture of the IPS.

In this work, the studied system is composed of two areas interconnected through a contact line, as shown in the underlying control architecture in Fig. 2. Area a contains the thermal power plants, ESS and loads, while area b includes the hydro power plants, PVA and loads. Moreover, more details about the mathematical modeling of the various devices within the studied IPS are described in the following subsections.

2.2 Generation system model

The generation system consists of the thermal power plants in area a and hydro power plants in area b. Among them, the thermal power plant model consists of governor $G_g(s)$, steam turbine $G_t(s)$ and reheater $G_r(s)$ [32], and their transfer functions can be described as:

$$G_g(s) = \frac{1}{T_g s + 1} \tag{1}$$

$$G_t(s) = \frac{1}{T_t s + 1} \tag{2}$$

$$G_r(s) = \frac{K_r T_r s + 1}{T_r s + 1} \tag{3}$$

where T_g, T_t and T_r denote the respective time constants of the governor, turbine and reheater of the thermal power plants [32]. K_r is the gain of the reheater of the thermal power plants.

Consequently, the transfer function of the thermal power plants model $G_{tp}(s)$ can be expressed as:

$$G_{tp}(s) = \frac{1}{T_g s + 1} \cdot \frac{1}{T_t s + 1} \cdot \frac{K_r T_r s + 1}{T_r s + 1} \tag{4}$$

In addition, the hydro power plants model is composed of governor $G_{hg}(s)$, droop compensation $G_{hd}(s)$ and pressure turbine $G_{ht}(s)$ [37], and their transfer functions can be written as:

$$G_{hg}(s) = \frac{1}{T_{gh} s + 1} \tag{5}$$

$$G_{hd}(s) = \frac{T_{rs} s + 1}{T_{rh} s + 1} \tag{6}$$

$$G_{ht}(s) = \frac{-T_w s + 1}{0.5 T_w s + 1} \tag{7}$$

where T_{gh}, T_{rs}, T_{rh} and T_w are the governor, transient sag, and reset time constants, and the nominal start time of water in the pressure main of the hydro power plants, respectively [37].

Thus, the transfer function of the hydro power plants model $G_h(s)$ can be described as:

$$G_h(s) = \frac{1}{T_{gh} s + 1} \cdot \frac{T_{rs} s + 1}{T_{rh} s + 1} \cdot \frac{-T_w s + 1}{0.5 T_w s + 1} \tag{8}$$

2.3 Model of PVA

PVA adopts information and communication technology with inverters to control the photovoltaic cells in series and parallel to meet the frequency regulation requirements of the IPS. The relationship between the terminal voltage and current of photovoltaic cells is nonlinear, and is affected by light radiation and temperature. To enhance the output power of the PVA, the conductance increment method is employed to achieve maximum power tracking. In view of this, the model of the PVA from [32] is used in this paper, and its transfer function is:

$$G_{PVA}(s) = \frac{K_{PV1} s + K_{PV2}}{s^2 + T_{PV1} s + T_{PV2}} \tag{9}$$

where K_{PV1} and K_{PV2} are the gains of the PVA, while T_{PV1} and T_{PV2} denote the respective time constants of the PVA.

2.4 Model of ESS

In recent years, capacitive energy storage has received extensive attention in its application in modern power systems. Capacitive energy storage exhibits advantages such as fast charging/discharging and response time, long operational life, needing no maintenance and being environmental friendly [6]. Consequently, capacitive energy storage is a high performance energy storage device which can play a significant role in enhancing the stability of power systems. Thus, in this paper capacitive energy storage is equipped in area a to guarantee the improvement of the system dynamic performance and mitigate the system frequency deviation. The mathematical model of the power increment variation of capacitive energy storage is:

$$\Delta P_{ESS} = \frac{T_1 s + 1}{T_2 s + 1} \cdot \frac{T_3 s + 1}{T_4 s + 1} \cdot \frac{K_{ESS}}{T_{ESS} s + 1} \cdot \Delta f_1 \tag{10}$$

where T_1, T_2, T_3 and T_4 are the respective time constants of the two-stage phase compensation module. K_{ESS} denotes the gain, T_{ESS} is the time constant of the capacitive energy storage [6], and Δf_1 denotes the frequency deviation of area a.

2.5 Model of contact line for IPS

In the studied system, the contact lines for connecting the two areas can enhance the dynamic performance of the IPS. A mathematical model of the contact line power deviation ΔP_{tie} between area a and area b is [37]:

$$\Delta P_{tie} = \frac{2\pi T_{tie}}{s}(\Delta f_1 - \Delta f_2) \tag{11}$$

where T_{tie} is the synchronization coefficient among areas, and Δf_2 denotes the frequency deviation of area b.

2.6 State space frequency model of IPS

The proposed frequency response model of the IPS is constructed by integrating the above models, as shown in Fig. 3. From the models, the state space frequency model of the system is derived. In this model, the time delay takes place in the communication channel that transmits the frequency response commands to the control devices.

Remark 2 It should be noted that the actual power system model is dynamic and nonlinear. In normal operation, only small changes in load are expected. Hence it assumes that the dynamic model of the studied system is linear in dealing with the LFC problem [26].

To begin with, by combining the dynamic models of various devices in area a and area b with the interconnected contact line model, a complete state space model of the IPS without considering delay is constructed, as shown in Fig. 3. The model and its parameters are:

$$\dot{x}(t) = Ax(t) + B_u u(t) + B_w w(t) \tag{12}$$

$$y(t) = Cx(t) \tag{13}$$

where $x(t)$, $y(t)$, $u(t)$ and $w(t)$ are the state, output, control and perturbation vectors of the system, respectively. A, B_u, B_w and C denote the system, control, perturbation and output matrices. More details of the above vectors and matrices can be found in (14–21).

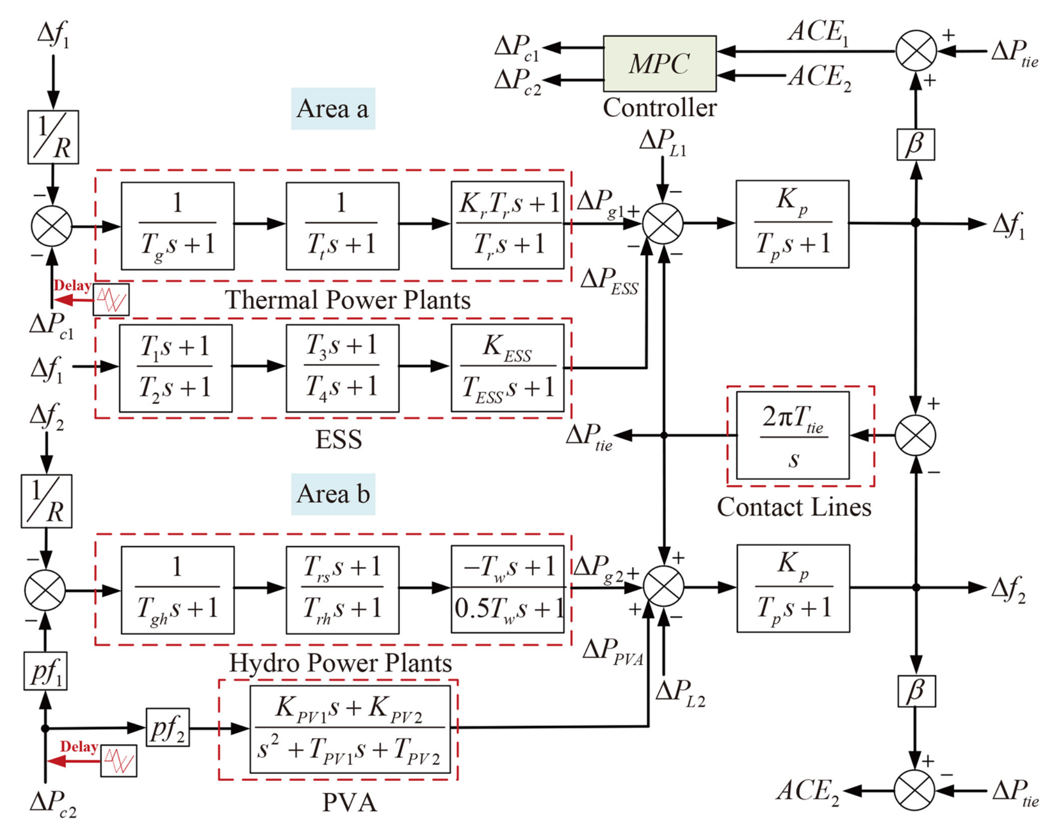

Fig. 3 The frequency response model of the studied IPS

$$x(t) = \left[\Delta f_1 \ \ \Delta P_{ESS} \ \ \Delta P_1 \ \ \Delta P_2 \ \ \Delta P_{g1} \ \ \Delta P_3 \ \ \Delta P_4 \ \ \Delta P_{tie} \ \ \Delta f_2 \ \ \Delta P_{PVA} \ \ \Delta P_5 \ \ \Delta P_{g2} \ \ \Delta P_6 \ \ \Delta P_7 \right]^T \tag{14}$$

$$u(t) = \left[\Delta P_{c1} \ \ \Delta P_{c2} \right]^T \tag{15}$$

$$w(t) = \left[\Delta P_{L1} \ \ \Delta P_{L2} \right]^T \tag{16}$$

$$y(t) = \left[\Delta f_1 \ \ ACE_1 \ \ \Delta f_2 \ \ ACE_2 \right]^T \tag{17}$$

with $A_{\sim}$ and $B_{\sim}$ in the control matrix are presented in the Appendix.

The linear discrete time state model is obtained by discretizing the continuous time model in (12) and (13) as:

$$x(k+1) = A_1 x(k) + B_{u1} u(k) + B_{w1} w(k) \tag{22}$$

$$A = \begin{bmatrix} -\frac{1}{T_p} & -\frac{K_p}{T_p} & 0 & 0 & \frac{K_p}{T_p} & 0 & 0 & -\frac{K_p}{T_p} & 0 & 0 & 0 & 0 & 0 & 0 \\ A_{2,1} & 0 & 1 & 0 & 0 & 0 & 0 & 0 & 0 & 0 & 0 & 0 & 0 & 0 \\ A_{3,1} & 0 & 0 & 1 & 0 & 0 & 0 & 0 & 0 & 0 & 0 & 0 & 0 & 0 \\ A_{4,1} & A_{4,2} & A_{4,3} & A_{4,4} & 0 & 0 & 0 & 0 & 0 & 0 & 0 & 0 & 0 & 0 \\ A_{5,1} & 0 & 0 & 0 & 0 & 1 & 0 & 0 & 0 & 0 & 0 & 0 & 0 & 0 \\ A_{6,1} & 0 & 0 & 0 & 0 & 0 & 1 & 0 & 0 & 0 & 0 & 0 & 0 & 0 \\ A_{7,1} & 0 & 0 & 0 & A_{7,5} & A_{7,6} & A_{7,7} & 0 & 0 & 0 & 0 & 0 & 0 & 0 \\ 2\pi T_{tie} & 0 & 0 & 0 & 0 & 0 & 0 & 0 & -2\pi T_{tie} & 0 & 0 & 0 & 0 & 0 \\ 0 & 0 & 0 & 0 & 0 & 0 & 0 & \frac{K_p}{T_p} & -\frac{1}{T_p} & \frac{K_p}{T_p} & 0 & \frac{K_p}{T_p} & 0 & 0 \\ 0 & 0 & 0 & 0 & 0 & 0 & 0 & 0 & 0 & 0 & 1 & 0 & 0 & 0 \\ 0 & 0 & 0 & 0 & 0 & 0 & 0 & 0 & 0 & -T_{PV2} & -T_{PV1} & 0 & 0 & 0 \\ 0 & 0 & 0 & 0 & 0 & 0 & 0 & 0 & A_{12,9} & 0 & 0 & 0 & 1 & 0 \\ 0 & 0 & 0 & 0 & 0 & 0 & 0 & 0 & A_{13,9} & 0 & 0 & 0 & 0 & 1 \\ 0 & 0 & 0 & 0 & 0 & 0 & 0 & 0 & A_{14,9} & 0 & 0 & A_{14,12} & A_{14,13} & A_{14,14} \end{bmatrix} \tag{18}$$

$$B_u = \begin{bmatrix} 0 & 0 & 0 & 0 & B_{1,5} & B_{1,6} & B_{1,7} & 0 & 0 & 0 & 0 & 0 & 0 & 0 \\ 0 & 0 & 0 & 0 & 0 & 0 & 0 & 0 & 0 & B_{2,10} & B_{2,11} & B_{2,12} & B_{2,13} & B_{2,14} \end{bmatrix}^T \tag{19}$$

$$B_w = \begin{bmatrix} -\frac{K_p}{T_p} & 0 & 0 & 0 & 0 & 0 & 0 & 0 & 0 & 0 & 0 & 0 & 0 & 0 \\ 0 & 0 & 0 & 0 & 0 & 0 & 0 & 0 & -\frac{K_p}{T_p} & 0 & 0 & 0 & 0 & 0 \end{bmatrix}^T \tag{20}$$

$$C = \begin{bmatrix} 1 & 0 & 0 & 0 & 0 & 0 & 0 & 0 & 0 & 0 & 0 & 0 & 0 & 0 \\ \beta & 0 & 0 & 0 & 0 & 0 & 0 & 1 & 0 & 0 & 0 & 0 & 0 & 0 \\ 0 & 0 & 0 & 0 & 0 & 0 & 0 & 0 & 1 & 0 & 0 & 0 & 0 & 0 \\ 0 & 0 & 0 & 0 & 0 & 0 & 0 & -1 & \beta & 0 & 0 & 0 & 0 & 0 \end{bmatrix} \tag{21}$$

In (14–21), ΔP_{g1}, ΔP_{g2} and ΔP_{PVA} denote the changes of power output provided by the thermal and hydro power plants and PVA, respectively. ΔP_{c1} and ΔP_{c2} are the respective control signals of areas a and b, while ΔP_{L1} and ΔP_{L2} denote load disturbances of areas a and b, respectively. ACE_1 and ACE_2 are the respective area control error signals for areas a and b, while pf_1 and pf_2 are the distribution participation factors of the hydro power plants and PVA, respectively. K_p and T_p are the gain and time constant of the generator, and β denotes the frequency deviation coefficient. To derive the linear state space model of the system, $\Delta P_{1\sim 7}$ are introduced as auxiliary variables. More details about the system matrices

$$y(k) = Cx(k) \tag{23}$$

where $A_1 = e^{AT_p}$, $B_{u1} = \int_0^{T_p} e^{A\tau} B_u d\tau$, $B_{w1} = \int_0^{T_p} e^{A\tau} B_w d\tau$, and T_p is the sample time.

Subsequently, the MPC-based controller is used based on the above model to reduce the system frequency deviation, contact line power deviation and area control error, and maintain the stability of the IPS. More detail can be found in the following sections.

3 Controller design and delay compensation strategy considering model uncertainty

In this section, the MPC-based LFC strategy for the IPS is first proposed. Considering the system model uncertainty, the Kalman filter is adopted to provide state estimation. Finally, combined with MPC, the delay compensation strategy is introduced to tackle the time delay and enhance the robustness of the IPS frequency regulation.

3.1 MPC-based load frequency control strategy

In industrial processes, MPC has been widely applied. Thus this subsection mainly discusses the application of MPC to the IPS for computing the future optimal frequency response commands of the system control devices by optimizing the proposed objective function. The theory on MPC is not described in detail here, and the related contents can be found in [32].

Definition 1 For illustration, $x(k+1|k)$ denotes the state of the system predicted for the future moment $(k+1)$ based on the state $x(k)$ at time k. p and c are the numbers of prediction and control steps, respectively, and $c \le p$.

Based on the above model in (22) and (23), the following equations are derived:

$$X(k) = A_2 x(k) + B_{u2} U(k) + B_{w2} W(k) \tag{24}$$

$$Y(k+1) = F_x x(k) + F_u U(k) + F_w W(k) \tag{25}$$

where $X(k) = \begin{bmatrix} x(k+1|k) \\ x(k+2|k) \\ \vdots \\ x(k+p|k) \end{bmatrix}$, $Y(k+1) = \begin{bmatrix} y(k+1|k) \\ y(k+2|k) \\ \vdots \\ y(k+p|k) \end{bmatrix}$,

$U(k) = \begin{bmatrix} u(k|k) \\ u(k+1|k) \\ \vdots \\ u(k+c-1|k) \end{bmatrix}$, $W(k) = \begin{bmatrix} w(k|k) \\ w(k+1|k) \\ \vdots \\ w(k+p-1|k) \end{bmatrix}$,

$A_2 = \begin{bmatrix} A_1 \\ A_1^2 \\ \vdots \\ A_1^p \end{bmatrix}$, $B_{u2} = \begin{bmatrix} B_{u1} & 0 & \cdots & 0 \\ A_1 B_{u1} & B_{u1} & \cdots & 0 \\ \vdots & \vdots & \ddots & \vdots \\ A_1^{p-1} B_{u1} & A_1^{p-2} B_{u1} & \cdots & A_1^{p-c} B_{u1} \end{bmatrix}$,

$B_{w2} = \begin{bmatrix} B_{w1} & 0 & \cdots & 0 \\ A_1 B_{w1} & B_{w1} & \cdots & 0 \\ \vdots & \vdots & \ddots & \vdots \\ A_1^{p-1} B_{w1} & A_1^{p-2} B_{w1} & \cdots & A_1 B_{w1} \end{bmatrix}$,

$C_1 = diag \overbrace{\begin{bmatrix} C & C & \cdots \end{bmatrix}}^{p}$, $F_x = C_1 A_2$, $F_u = C_1 B_{u2}$, and $F_w = C_1 B_{w2}$.

Remark 3 Note that both the initial state and the perturbation can be obtained by the sensors of the system. Hence, we assume them to be known.

The optimized objective function of the MPC-based controller to guarantee the stability of the system frequency is:

$$\begin{aligned} \underbrace{\min}_{u(k|k),\ldots,u(k+c-1|k)} \quad & J = \sum_{n=1}^{p} \left\| y(k+n|k) - y_r \right\|_W^2 + \\ & \sum_{n=1}^{c} \left\| u(k+n-1|k) \right\|_V^2 \\ s.t.\ & u_{\min}(k+i|k) \le u(k+i|k) \le u_{\max}(k+i|k) \\ & \Delta u_{\min}(k+i|k) \le \Delta u(k+i|k) \le \Delta u_{\max}(k+i|k) \\ & i = 0, 1, \cdots, c-1 \end{aligned} \tag{26}$$

where W and V are the diagonal matrices of weight coefficients. y_r is the output reference value of the system frequency deviation and area control error, which is set to 0 in this paper. $\Delta u(k+i|k) = u(k+i|k) - u(k+i-1|k)$.

Equation (26) is rewritten in matrix form as:

$$\begin{aligned} & \underbrace{\min}_{U} J(U(k)) = U(k)^T H U(k) + I(k) U(k) \\ & s.t.\ U_{\min} \le U(k) \le U_{\max} \\ & \quad \left| \Delta U(k) \right| \le \Delta U_{\max} \end{aligned} \tag{27}$$

where $H = F_u^T W F_u + V$, $I(k) = 2(x(k)^T F_x^T + W(k)^T F_w^T) W F_u$, $U_{\min} = \overbrace{\begin{bmatrix} m_1 & m_1 & \cdots & m_1 \end{bmatrix}}^{2c}{}^T$,

$U_{\max} = \overbrace{\begin{bmatrix} m_2 & m_2 & \cdots & m_2 \end{bmatrix}}^{2c}{}^T$,

$\Delta U(k) = \begin{bmatrix} \Delta u(k|k) \\ \Delta u(k+1|k) \\ \vdots \\ \Delta u(k+c-1|k) \end{bmatrix}$,

$\Delta U_{\max} = \overbrace{\begin{bmatrix} m_3 & m_3 & \cdots & m_3 \end{bmatrix}}^{2c}{}^T$, and.

m_1, m_2 and m_3 denote the lower and upper limits of the system control input, and the upper limit of the input variation, respectively. More details on the derivation process of H and $I(k)$ in (27) are presented in Appendix.

Additionally, contact line power deviation of the system should not exceed its limit during IPS frequency control according to the safety and stability guidelines. Thus a safety constraint of contact line power deviation also needs to be considered in the MPC optimization process, described as:

$$m_4 \le \Delta P_{tie} \le m_5 \tag{28}$$

where m_4 and m_5 are the minimum and maximum power fluctuation deviation values of the contact line, respectively.

It is then rewritten into the following matrix form:

$$ZU(k) \le z \tag{29}$$

where $Z = \begin{bmatrix} -SB_{u2} \\ SB_{u2} \end{bmatrix}$,

$z = \begin{bmatrix} SA_2 x(k) + SB_{w2} W(k) - M_4 \\ -SA_2 x(k) - SB_{w2} W(k) + M_5 \end{bmatrix}$,

$S = diag \overbrace{\begin{bmatrix} S_g & S_g & \cdots & S_g \end{bmatrix}}^{p}$,

$S_g = \begin{bmatrix} 0 & 0 & 0 & 0 & 0 & 0 & 0 & 1 & 0 & 0 & 0 & 0 & 0 & 0 \end{bmatrix}$,

$M_4 = diag\left[\overbrace{m_4\ m_4\ \cdots\ m_4}^{p}\right]^T$,

$M_5 = diag\left[\overbrace{m_5\ m_5\ \cdots\ m_5}^{p}\right]^T$, and.

M_4 and M_5 denote the lower and upper bounds constructed from (28), respectively.

Finally, at each time period k, the optimal sequence of control input variables is derived by minimizing the objective function and its constraints (27) and (29) as:

$$U^*(k) = \begin{bmatrix} u^*(k|k) \\ u^*(k+1|k) \\ \vdots \\ u^*(k+c-1|k) \end{bmatrix} \tag{30}$$

Remark 4 It is worth noting that only the first element of the optimal sequence, i.e., $u^*(k|k)$ is used for the system frequency deviation control. The stability and robustness of the IPS can be effectively improved through establishing the proposed LFC model and executing the optimal control sequence to handle the system frequency problem.

3.2 Kalman filter based system state estimation method

In order to cope with system model uncertainty, the Kalman filter is employed to estimate the state of $x(k)$ in (31) and (32) to further enhance the reliability of the PCM. Consequently, based on the above model in (22) and (23), the mathematical model considering uncertainty is:

$$x(k+1) = A_1x(k) + B_{u1}u(k) + B_{w1}w(k) + B_\sigma\sigma(k) \tag{31}$$

$$y(k) = Cx(k) + v(k) \tag{32}$$

where $\sigma(k)$ and $v(k)$ denote the zero-mean system process and the measured white noise, respectively.

Based on the model in (31) and (32), the state estimation correction is:

$$\begin{aligned}\hat{x}(k|k) = {} & A_1x(k-1|k-1) + B_{u1}u(k-1) + B_{w1}w(k-1) + \\ & K(k)\cdot\left[y(k) - C(A_1\hat{x}(k-1|k-1) + \right. \\ & \left. B_{u1}u(k-1) + B_{w1}w(k-1))\right]\end{aligned} \tag{33}$$

where $\hat{x}(k|k)$ is the state estimate of $x(k)$ at time k, $K(k) = P^-(k)C^T(CP^-(k)C^T + R)^{-1}$,

$P^-(k) = A_1P(k-1)A_1^T + Q$,

$P(k) = (I - K(k)C)P^-(k)$, and.

$K(k)$ is the optimal Kalman gain at time k. $P^-(k)$ and $P(k)$ denote the prior and posterior state estimation covariances, respectively. Q and R are the covariance matrices of $\sigma(k)$ and $v(k)$, respectively, and I is the unit matrix with appropriate dimensions.

Subsequently, $\hat{x}(k)$ is applied to modify $x(k)$ in (27) to improve prediction accuracy and system stability.

Remark 5 It should be noted that before employing the Kalman filter, the following set of assumptions should be satisfied, i.e.: the previously mentioned system dynamic model is linear, and the system processes and the measured noise are independent of each other while both obey the Gaussian distribution.

3.3 Delay compensation strategy

In this subsection, the MPC-based prediction compensation strategy in [38] is introduced to eliminate the delay problem. To facilitate the description, the following assumptions and definitions are made.

Remark 6 It is worth noting that in the studied system, it is assumed that the clocks of the relevant control components such as sensors, controllers and delay compensators are configured to meet the synchronization conditions and operate in a time-driven manner [38]. All control devices are equipped with a "memory" module to store the control signals computed by the MPC-based controller at each time. The resulting optimal control sequence (30) is encapsulated in a data packet at each time point, and a time stamp is marked to determine the delay impact.

Definition 2 τ denotes the transmission delay, $0 \le \tau \le d_mT_p$, and d_m is a positive integer with $d_m \le p$.

The main content of the proposed PCM in this paper is that the delay compensator of the system control end selects $k-i$ at time k as the optimal control input sequence $U^*(k-i)$ acting on the control equipment to compensate for the effect of delay. The specific description of the proposed strategy is as follows:

It is assumed that the system optimal control sequence $U^*(k-i)$ can be calculated at time $k-i$, and then arrives at the device control end after time delay $\tau_{k-i}(i = 0, 1, \cdots, d_m)$. Thus, the arrival time of the control sequence is $k - i + \tau_{k-i}$. Assuming that all packets satisfying condition $\tau - i \le 0$ reach the device control at time k:

$$\sigma_i = \min\{i|\tau_{k-i} - i \le 0\}, i = 0, 1, \cdots, d_m \tag{34}$$

Based on the above description, the control instruction selected to act on the device at time k is:

$$U^*(k|k-i) = [\overbrace{0 \cdots 0}^{\tau_{k-i}} \; I \cdots 0]U^*(k-i) \tag{35}$$

Remark 7 Note that there exists network connection between the control center and the device console. Input control commands frequently undergo time delay in the transmission channel. This is the reason for emphasizing the compensation strategy to eliminate the effect of delay [30].

3.4 Stability analysis

To illustrate that the proposed control method can ensure stable operation of the system, it is necessary to further analyze the stability of the system.

The stability of the studied system (22)-(23) can be analyzed by the switched system method. More detailed description of the stability analysis can be found in [38].

4 Simulation results

In this section, the effectiveness of the proposed MPC-based control strategy is proved via two case studies based on the IPS model illustrated in Fig. 3. The system parameters adopted in the simulation refer to the relevant data in [6, 32]. For simplicity, $p = c = 25$, and the sampling time T_p is 0.1 s. The simulation environment is MATLAB/Simulink on a PC with AMD Ryzen 5 3550H CPU, 16 GB of RAM, and a 64-bit operating system.

4.1 Simulation results excluding model uncertainty

In this case, all simulation results are conducted excluding

the model uncertainty. The effectiveness of the proposed method is verified in the following four scenarios by combining the system responses and its performance comparison results between the proposed control method and PI control in [10, 35].

4.1.1 Load change

In this scenario (scenario 1), two different cases of load change in the IPS are considered. Case 1: area a is subjected to step load disturbance, and case 2: area b is exposed to random step load disturbance, as illustrated in Figs. 4 (a) and (b), respectively. The simulation time of the two situations is 50 s and 150 s, respectively. The response results of the IPS for the step load disturbance applied on area a and the random step load disturbance applied on area b are shown in Figs. 5 and 6, respectiv ely.

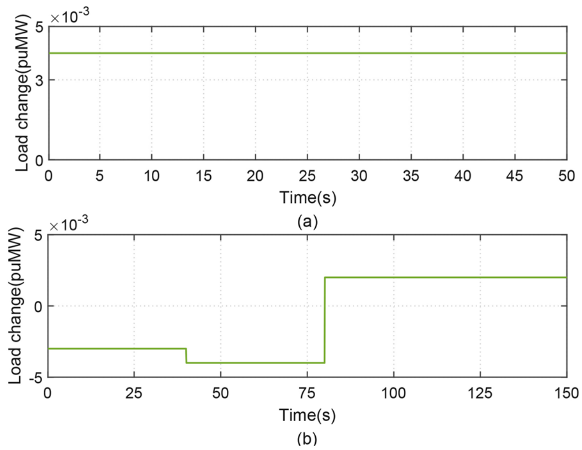

Fig. 4 The load profiles for scenario 1 (case 1). **a** Step load disturbance for area a; **b** Variable load disturbance for area b

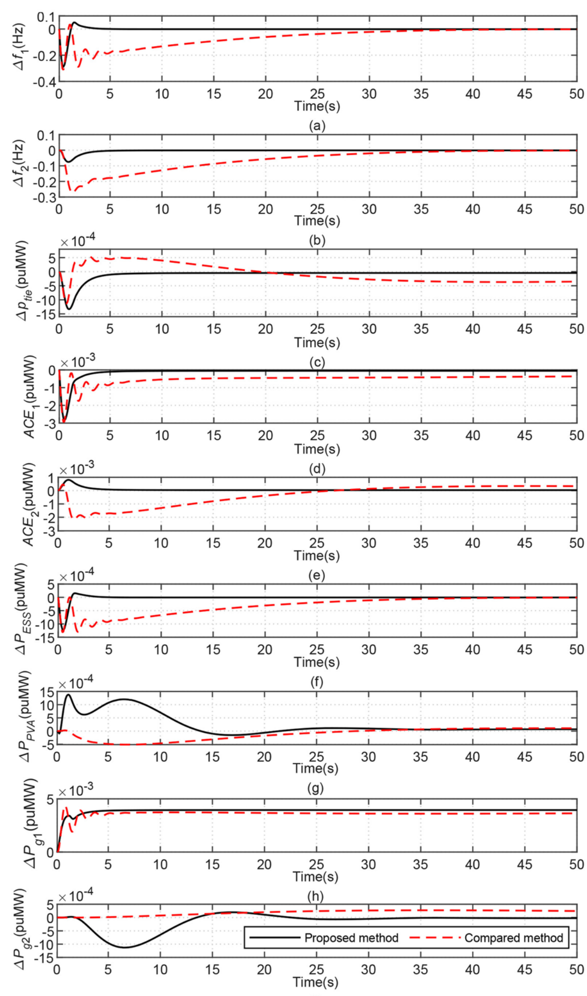

Fig. 5 Responses of the IPS for step load disturbance applied on area a for scenario 1 (case 1). **a** Δf_1, **b** Δf_2, **c** ΔP_{tie}, **d** ACE_1, **e** ACE_2, **f** ΔP_{ESS}, **g** ΔP_{PVA}, **h** ΔP_{g1} and **i** ΔP_{g2}

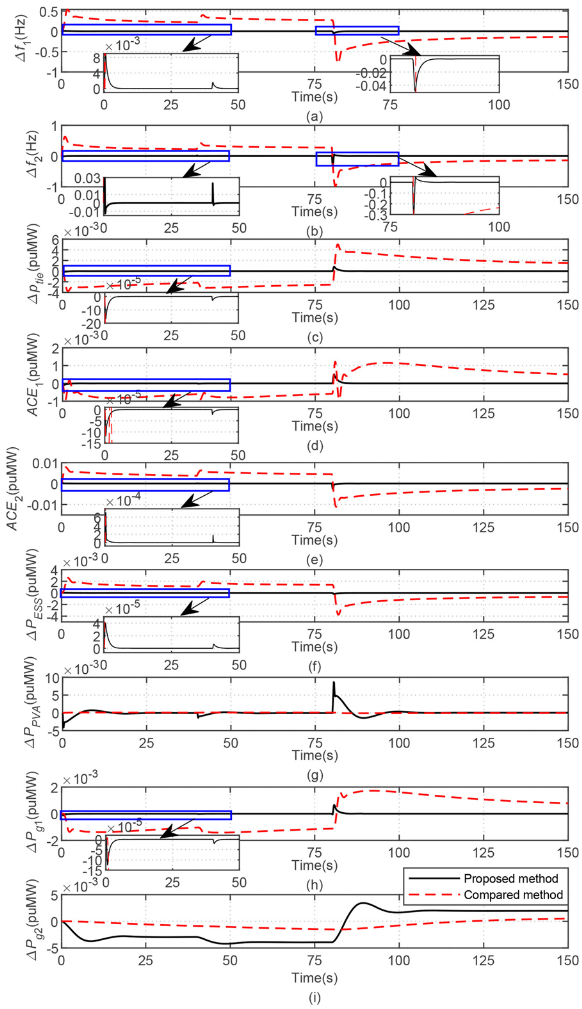

Fig. 6 Responses of the IPS for variable step load disturbance applied on area b for scenario 1 (case 2). **a** Δf_1, **b** Δf_2, **c** ΔP_{tie}, **d** ACE_1, **e** ACE_2, **f** ΔP_{ESS}, **g** ΔP_{PVA}, **h** ΔP_{g1} and **i** ΔP_{g2}

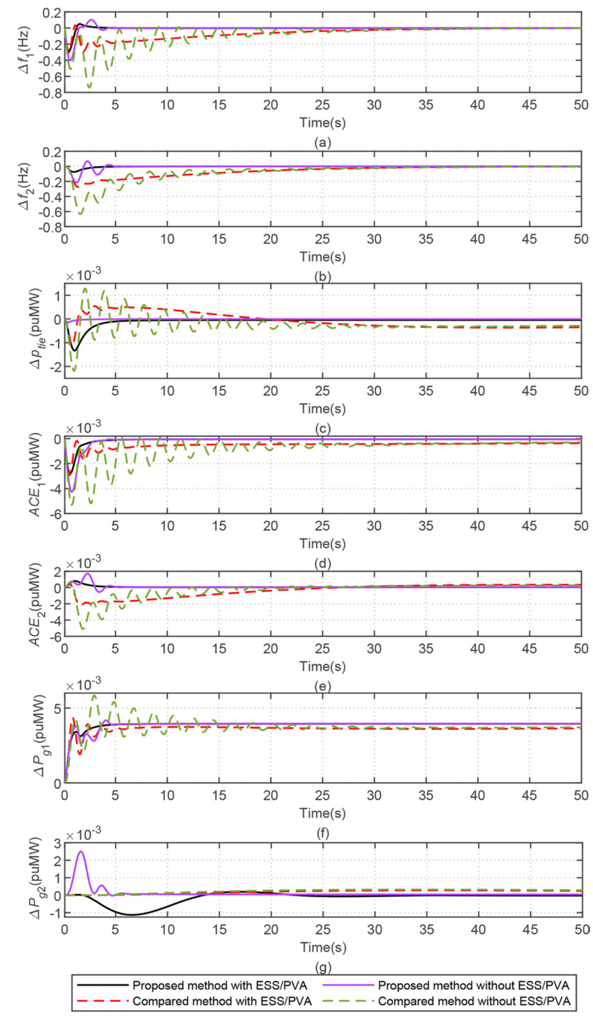

Fig. 7 Comparative responses of the IPS with ESS/PVA for step load disturbance applied on area a for scenario 2 (case 1). **a** Δf_1, **b** Δf_2, **c** ΔP_{tie}, **d** ACE_1, **e** ACE_2, **f** ΔP_{ESS}, **g** ΔP_{PVA}, **h** ΔP_{g1} and **i** ΔP_{g2}

As shown in Figs. 5 and 6, after the IPS is disturbed for load changes, the frequency deviation, contact line power deviation and area control error are properly adjusted because of the use of the controller to flexibly control the system equipment. It can be seen that the method can regulate the frequency deviation, contact line power deviation and area control error to stability, but there are steady-state errors, a long response time and low flexibility of equipment invocation.

4.1.2 Simulation considering ESS/PVA

In this scenario (scenario 2), the effectiveness of the proposed method is validated based on the IPS model shown in Fig. 3. The comparative performance with the PI method and the situation excluding ESS/PVA is also provided. The system model excluding ESS/PVA is simulated in the same scenario as in scenario 1 where area a is subjected to the step load disturbance.

The comparison results of the IPS response considering ESS/PVA for step load disturbance applied on area a are illustrated in Fig. 7. It can be seen that excluding ESS/PVA, the proposed method is more effective in suppressing frequency deviation, contact line power deviation and area control error, to some extent, than the compared method.

Nevertheless, they suffer from certain oscillations in frequency deviation, contact line power fluctuation and area control error regulation during system disturbance, and the response time is also long. Considering ESS/PVA, it can be clearly seen that they both enable the coordination of ESS and PVA to achieve the attenuation of frequency deviation with area control error and the reduction of system response time. It should also be

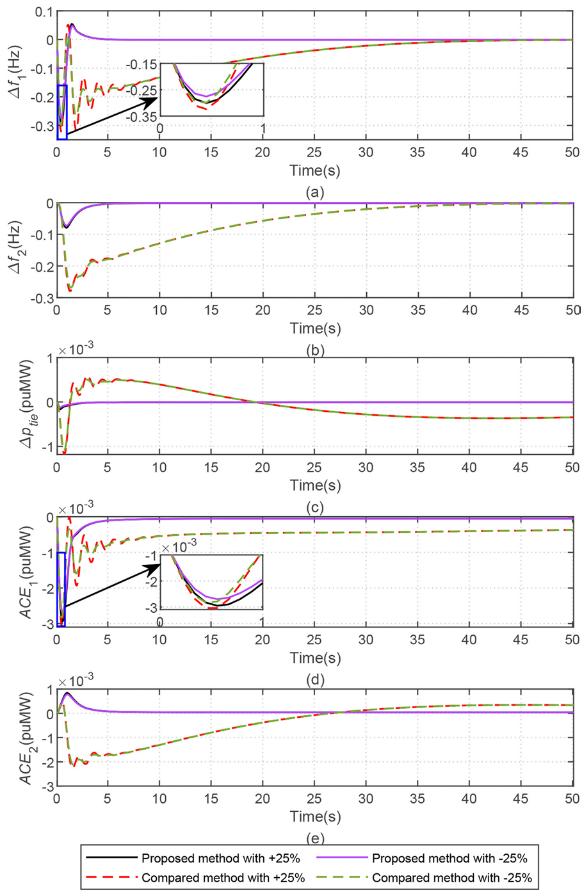

Fig. 8 Responses of the IPS with parameters variations for step load disturbance applied on area a for scenario 3 (case 1). **a** Δf_1, **b** Δf_2, **c** ΔP_{tie}, **d** ACE_1 and **e** ACE_2

noted that the proposed method has superior robustness in the coordination of ESS and PVA compared with the PI method.

4.1.3 Robustness analysis

In this scenario (scenario 3), the robustness of the proposed method is verified by varying some parameters (e.g., T_g, K_{PV1} and T_{ESS}) of the thermal power plants, PVA and ESS in the IPS based on scenario 1, where area a is subjected to the step load disturbance. The comparative performance is provided for the situations where the above parameters are increased and decreased by 25%, while the other parameters remain unchanged. The response results for the.

parameter changes of the IPS for the step load disturbance applied to area a are illustrated in Fig. 8.

As illustrated in Fig. 8, the proposed method demonstrates better performance than the compared method in response to system parameter variations. It can effectively reduce the maximum frequency deviation, contact line power deviation and area control error, and shorten the response regulation time. Consequently, the proposed method is proved to be robust to system parameter variations.

4.1.4 Simulation considering time delay

In this scenario (scenario 4), communication delays of 0.2 s and 0.4 s are considered to verify the performance of the proposed method and PCM based on scenario 1 where area a is subjected to the step load disturbance. The comparative performances with the PI method and the situation without PCM are provided. The response results of the IPS considering time delay and PCM for step load disturbance applied to area a are shown in Figs. 9 and 10, respectively. As shown in Fig. 9, the frequency deviation, contact line power deviation and area control error increase as the delay grows for both methods. Nevertheless, the proposed method enables lower frequency deviation than the compared method. As illustrated in Fig. 10, it can be noted that the frequency deviation, contact line power deviation and

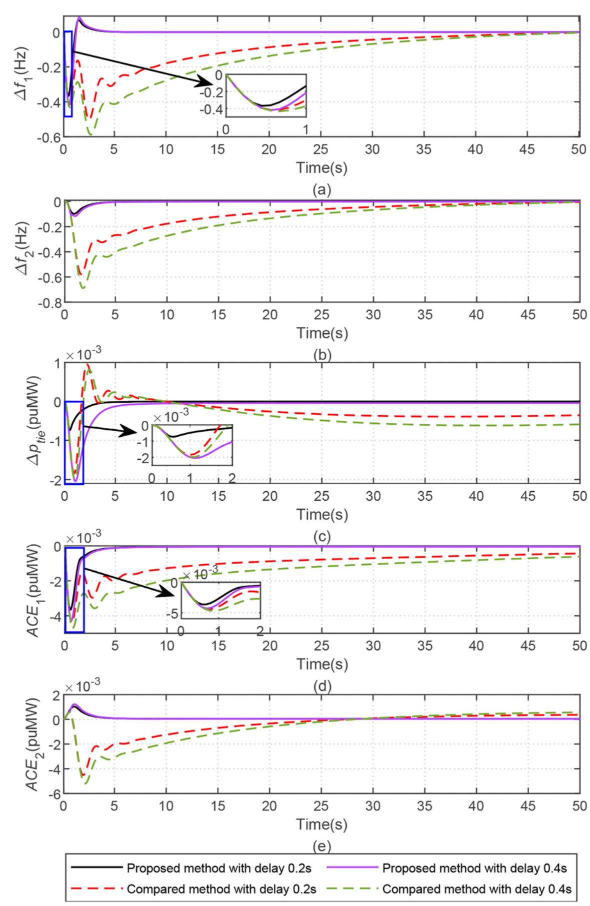

Fig. 9 Responses of the IPS with time delay for step load disturbance applied on area a for scenario 4 (case 1). **a** Δf_1, **b** Δf_2, **c** ΔP_{tie}, **d** ACE_1 and **e** ACE_2

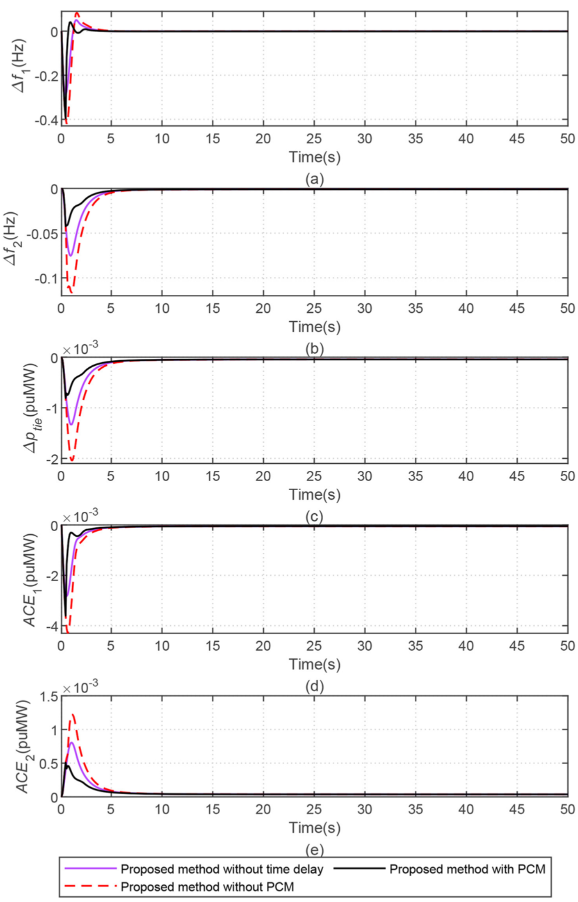

Fig. 10 Responses of the IPS with PCM for step load disturbance applied on area a for scenario 4 (case 1). **a** Δf_1, **b** Δf_2, **c** ΔP_{tie}, **d** ACE_1 and **e** ACE_2

area control error increase to some extent when the system undergoes a time delay. Additionally, compared without PCM, more conservative results are obtained with PCM, which effectively reduces the frequency deviation, contact line power deviation and area control error, and enhances the stability of the system.

As mentioned above, the superiority of the proposed method in frequency regulation and the efficiency of the delay compensation strategy in eliminating the effect of time delay are confirmed.

4.1.5 Performance comparison

In this subsection, to further test the efficiency of the proposed method, the control performance of each method is measured by comparing the four widely applied performance indices, i.e., error square integral (ISE), integral absolute error (IAE), time multiplied error square integral (ITSE) and time multiplied error absolute value integral (ITAE). Their expressions are as follows:

$$ISE = \int_0^{t_s} ((\Delta f_1)^2 + (\Delta f_2)^2 + (\Delta P_{tie})^2)dt \tag{36}$$

$$IAE = \int_0^{t_s} (|\Delta f_1| + |\Delta f_2| + |\Delta P_{tie}|)d \tag{37}$$

$$ITSE = \int_0^{t_s} t((\Delta f_1)^2 + (\Delta f_2)^2 + (\Delta P_{tie})^2)dt \tag{38}$$

$$ITAE = \int_0^{t_s} t(|\Delta f_1| + |\Delta f_2| + |\Delta P_{tie}|)dt \tag{39}$$

where t_s is the duration of the statistic.

The performance indices of the different control methods for the different scenarios mentioned above are provided in Table 1. As seen, it is clear that the performance indices of the proposed method are smaller than those of the compared method, e.g., the proposed method has shorter response regulation time and better robustness in the studied scenarios.

Additionally, it should be noted that in scenario 4, the performance indices of the proposed method with the delay compensation strategy are lower than those of the compared method, which further verifies the superiority of the proposed PCM.

Table 1 Comparative analysis of performance indices for the different scenarios

Scenarios	Methods	Performance indices			
		ISE	IAE	ITSE	ITAE
No.1	Compared	0.8294	6.2448	5.8821	71.3548
(Case 1)	**Proposed**	**0.0509**	**0.4761**	**0.0320**	**2.9937**
No.1	Compared	22.4975	77.6274	1395.9515	5210.5255
(Case 2)	**Proposed**	**0.0293**	**0.2560**	**2.2240**	**17.2418**
No.2	Compared	2.0842	7.6199	9.0758	72.6244
	Proposed	**0.1544**	**0.8172**	**0.1452**	**2.0523**
No.3	Compared	0.8392	6.2576	5.8845	71.2832
(Case 1)	**Proposed**	**0.0550**	**0.4854**	**0.0344**	**2.9629**
No.3	Compared	0.8220	6.2355	5.8857	71.4290
(Case 2)	**Proposed**	**0.0470**	**0.4583**	**0.0297**	**2.9151**
2*No.4	Compared	4.1575	14.6230	30.8214	184.3838
	Proposed	**0.0389**	**0.3197**	**0.0167**	**2.7693**

Bold values indicate the best value of each performance indice in the different control methods

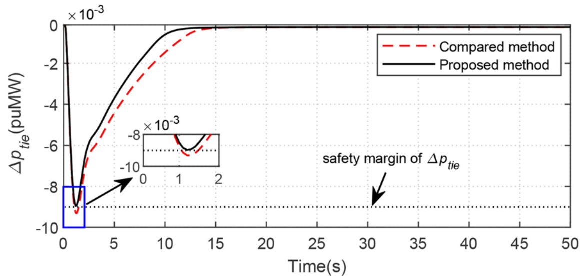

Fig. 11 Comparison of contact line power deviation responses of the IPS for step load disturbance applied on area a for scenario 5 (case 1)

4.1.6 Simulation considering contact lines power fluctuation limit

In this subsection, the safety of the proposed method is further confirmed through increasing the load disturbance based on scenario 1 (now called scenario 5) where area a is affected by the step load disturbance. The comparative performance with the method without considering the contact line power deviation limitation (compared method) is provided.

The comparative results of the contact line power deviation response of the IPS for step load perturbation applied to area a are illustrated in Fig. 11. It can be seen that the proposed method can effectively keep the contact line power fluctuation within the safe range, but the compared method fails to control the contact line power deviation.

4.2 Simulation results involving model uncertainty

In this case, the proposed method is evaluated involving model uncertainty, and the advantages of the proposed method in terms of frequency regulation are demonstrated by the following two scenarios.

4.2.1 Frequency control involving model uncertainty

In this scenario, the efficiency of the proposed method is verified involving model uncertainty based on the situation of the step load disturbance on area a of scenario 1 in case 1. The comparative performance with the MPC method without considering the model uncertainty (compared method) is provided. The response results of imposing step load disturbance on area a of the IPS considering model uncertainty are shown in Fig. 12.

As shown in Fig. 12, it can be seen that both control methods regulate the frequency deviation to stability after the system is disturbed, although a certain frequency deviation still exists with the compared method. The simulation results prove the effectiveness of the proposed method in frequency control.

4.2.2 PCM involving model uncertainty

In the same case of scenario 1 where area a is subjected to the step load disturbance, a communication delay 0.5 s is considered to verify the effectiveness of the proposed PCM involving model uncertainty. The comparison of the performance without the PCM (compared method 1) and without considering the model uncertainty (compared method 2) are provided.

The response results of the PCM involving model uncertainty for step load disturbance are illustrated in Fig. 13. It can be noted that the proposed method further reduces the frequency deviation of the IPS compared to the two comparison methods. Hence, according to the simulation results, the proposed method enhances the reliability of the system delay compensation.

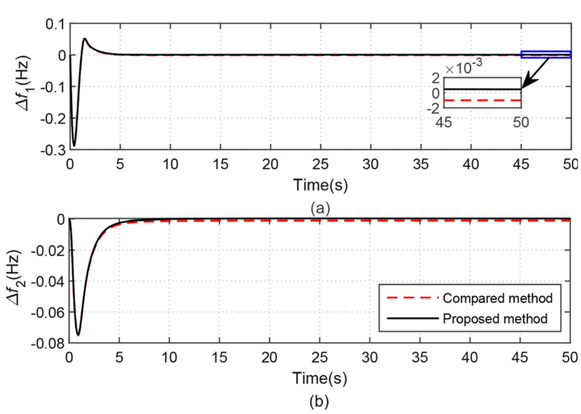

Fig. 12 Responses of the IPS involving model uncertainty for step load disturbance applied on area a for scenario 1 (case 1). **a** Δf_1 and **b** Δf_2

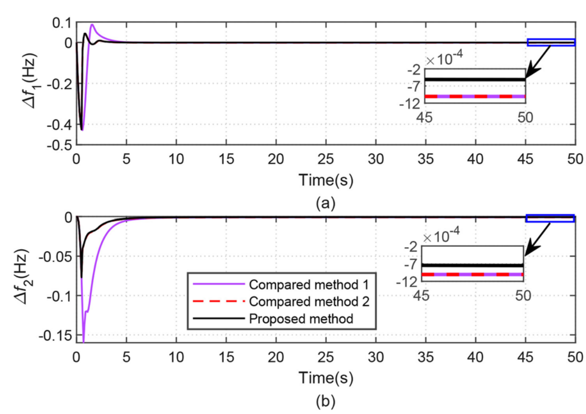

Fig. 13 Responses of the IPS with PCM involving model uncertainty for step load disturbance applied on area a for scenario 2 (case 1). **a** Δf_1 and **b** Δf_2

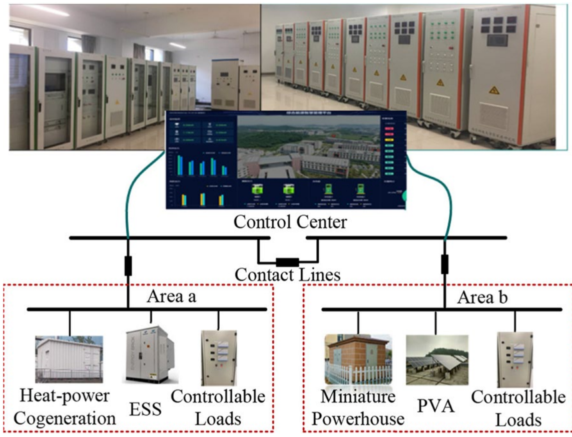

Fig. 14 Experimental test platform for LFC of the IPS

4.3 Effectiveness verification based on experimental platform

In this section, the effectiveness of the proposed MPC-based LFC strategy is verified based on an experimental test platform, shown in Fig. 14. The heat-power cogeneration and miniature powerhouse are used to simulate the role of the actual thermal power plants and hydro power plants, and the roof photovoltaic of the laboratory is used to simulate PVA. In addition, the ESS and controllable loads of the experimental platform are used to simulate the ESS and load deviation in the IPS. The control center is responsible for sending the control instructions and receiving the running data of the experimental tests.

In the experimental test, the experimental time-length is set to 300 s. The change of controllable loads in area a is used to simulate the load perturbations in the IPS, as shown in Fig. 15. In addition, the effectiveness of the proposed control method is verified in the experimental tests by combining the system response and its performance comparison results with PI control (compared method) [10, 35]. All the running data are processed, and the experimental results are generated by MATLAB.

The response experimental results of the IPS for the load disturbance are illustrated in Fig. 16. It can be seen that the proposed control method can better offset the influence of load disturbances. Especially, when the load fluctuates greatly at 60 s, 150 s and 270 s, the proposed method leads to lower load frequency deviation and area control error, with faster convergence. Furthermore, it can also be clearly seen that the proposed method has strong robustness and can effectively reduce the burden of the contact line.

In addition, the performance indices of the different control methods for the experimental tests are shown in Table 2. As shown, compared with the other method, the ISE of the proposed method is reduced by 93.26 %, the IAE is reduced by 84.21 %, the ITSE is reduced by 93.58 % and

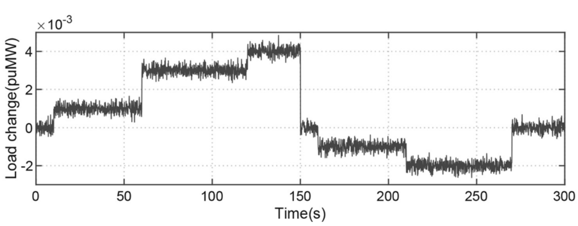

Fig. 15 The simulated load disturbance curve for controllable loads in area a

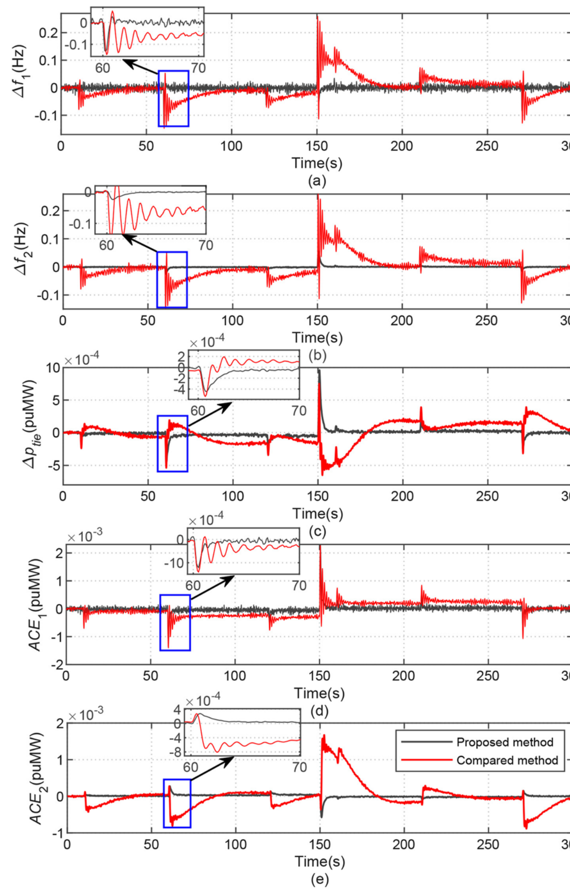

Fig. 16 Responses of the IPS for the load disturbance. **a** Δf_1, **b** Δf_2, **c** ΔP_{tie}, **d** ACE_1 and **e** ACE_2

Table 2 Comparative analysis of performance indices for the experimental test

Methods	Performance indices			
	ISE	IAE	ITSE	ITAE
Compared	0.9052	16.0562	136.5697	2448.3256
Proposed	**0.0610**	**2.5345**	**8.7696**	**373.8222**

Bold values indicate the best value of each performance indice in the different control methods the ITAE is reduced by 84.73 %. Thus, it demonstrates that the proposed method has shorter response adjustment time and better robustness in the experimental tests.

In summary, the above results and analysis show that the proposed control method can effectively offset the influence of load disturbance and make the grid load frequency deviation and area control error converge. The feasibility,

effectiveness and strong robustness of the proposed method are thus verified.

5 Conclusions

To address the frequency regulation problem in IPS, this paper proposes a cloud-edge-end coordination-based LFC architecture for the first time. This provides a unified cloud control center to coordinate the frequency regulation among different areas. An MPC-based LFC strategy for the IPS with PVA and ESS under model uncertainty and communication delay is proposed. First, a state space model of the IPS is presented, and the MPC-based controller and PCM considering model uncertainty are introduced to improve the robustness and security of the IPS. The simulation results show that the proposed strategy has superior performance in frequency control and time delay elimination compared with some baseline methods. Overall, the proposed frequency control architecture and strategy can provide certain reference values for the future development of IPS.

Appendix

The specific expressions of $A_{\sim}$ and $B_{\sim}$ in the proposed system matrices and control matrices are:

$$A_{2,1} = \frac{T_1 T_3 K_{ESS}}{T_2 T_4 T_{ESS}},$$

$$A_{3,1} = \frac{K_{ESS}(T_1 + T_3)}{T_2 T_4 T_{ESS}} - \frac{T_1 T_3 K_{ESS}[(T_2 + T_4)T_{ESS} + T_2 T_4]}{(T_2 T_4 T_{ESS})^2},$$

$$A_{4,1} = \frac{K_{ESS}}{T_2 T_4 T_{ESS}} - \frac{A_{3,1}[(T_2 + T_4)T_{ESS} + T_2 T_4]}{T_2 T_4 T_{ESS}} - \frac{T_1 T_3 K_{ESS}(T_2 + T_4 + T_{ESS})}{(T_2 T_4 T_{ESS})^2}$$

$$A_{4,2} = -\frac{1}{T_2 T_4 T_{ESS}},\ A_{4,3} = -\frac{T_2 + T_4 + T_{ESS}}{T_2 T_4 T_{ESS}},$$

$$A_{4,4} = -\frac{(T_2 + T_4)T_{ESS} + T_2 T_4}{T_2 T_4 T_{ESS}},$$

$$A_{5,1} = 0,\ A_{6,1} = -\frac{K_r}{T_g T_t R},$$

$$A_{7,1} = -\frac{T_g T_t - K_r[(T_g + T_t)T_r + T_g T_t]}{(T_g T_t)^2 T_r R},$$

$$A_{7,5} = -\frac{1}{T_g T_t T_r},\ A_{7,6} = -\frac{T_g + T_t + T_r}{T_g T_t T_r},$$

$$A_{7,7} = -\frac{(T_g + T_t)T_r + T_g T_t}{T_g T_t T_r},\ A_{12,9} = \frac{T_{rs}}{0.5 T_{gh} T_{rh} R}$$

$$A_{13,9} = -\frac{T_{rs} - T_w}{0.5 T_{gh} T_{rh} T_w R} - \frac{T_{rs}[0.5 T_w (T_{gh} + T_{rh}) + T_{gh} T_{rh}]}{(0.5 T_{gh} T_{rh})^2 T_w R},$$

$$A_{14,9} = -\frac{1}{0.5 T_{gh} T_{rh} T_w R} - \frac{A_{13,9}[0.5 T_w (T_{gh} + T_{rh}) + T_{gh} T_{rh}]}{0.5 T_{gh} T_{rh} T_w} - \frac{A_{12,9}(0.5 T_w + T_{gh} + T_{rh})}{0.5 T_{gh} T_{rh} T_w},$$

$$A_{14,12} = -\frac{1}{0.5 T_{gh} T_{rh} T_w},\ A_{14,13} = -\frac{0.5 T_w + T_{gh} + T_{rh}}{0.5 T_{gh} T_{rh} T_w}$$

$$A_{14,14} = -\frac{0.5 T_w (T_{gh} + T_{rh}) + T_{gh} T_{rh}}{0.5 T_{gh} T_{rh} T_w}.\ B_{1,5} = 0$$

$$B_{1,6} = R A_{6,1},\ B_{1,7} = R A_{7,1},\ B_{2,10} = pf_2 K_{PV1},$$

$$B_{2,11} = pf_2 (K_{PV2} - T_{PV1} K_{PV1}),$$

$$B_{2,12} = pf_1 R A_{12,9},\ B_{2,13} = pf_1 R A_{13,9},$$

$$B_{2,14} = pf_1 R A_{14,9}.$$

The derivation processes of H and $I(k)$ in (27) are specified as follows:

$$\begin{aligned}
&\sum_{n=1}^{p} \left\| y(k+n|k) - y_r \right\|_W^2 + \sum_{n=1}^{c} \left\| u(k+n-1|k) \right\|_V^2 = \\
&Y(k)^T W Y(k) + U(k)^T V U(k) = \\
&(F_x x(k) + F_u U(k) + F_w W(k))^T W (F_x x(k) + \\
&F_u U(k) + F_w W(k)) + U(k)^T V U(k) = \\
&x(k)^T F_x^T W F_u U(k) + U(k)^T F_u^T W F_x x(k) + \\
&U(k)^T F_u^T W F_u U(k) + U(k)^T F_u^T W F_w W(k) + \\
&W(k)^T F_w^T W F_u U(k) + U(k)^T V U(k) = \\
&U(k)^T (F_u^T W F_u + V) U(k) + \\
&[2 F_u^T W (F_x x(k) + F_w W(k))]^T U(k) = \\
&U(k)^T \underbrace{(F_u^T W F_u + V)}_{H} U(k) + \\
&\underbrace{[2(x(k)^T F_x^T + W(k)^T F_w^T) W F_u]}_{I(k)} U(k)
\end{aligned}$$

Abbreviations

IPS	Interconnected power systems
MPC	Model predictive control
LFC	Load frequency control
PVA	Photovoltaics aggregation
ESS	Energy storage systems
RESs	Renewable energy sources
PI	Proportional integral
SA	Simulated annealing
ABC	Artificial bee colony
CS	Cuckoo search
FACTS	Flexible alternating current transmission system
PCM	Predictive compensation mechanism

Acknowledgements
The author would especially like to express gratitude to the associate editor and anonymous reviewers for their valuable comments and suggestions to improve the quality of the paper. Also, the authors would like to thank the Hybrid AI and Big Data Research Center of Chongqing University of Education (2023XJPT02) for financial support, which made this research possible.

Author contributions
All authors read and approved the final manuscript.

Funding
The research was supported by Hybrid AI and Big Data Research Center of Chongqing University of Education (2023XJPT02).

Availability of data and materials
Please contact author for data and material request.

Declarations

Competing interests
The authors declare that they have no known competing financial interests or personal relationships that could have appeared to influence the work reported in this paper.

Received: 19 February 2023 Accepted: 21 September 2023
Published online: 12 October 2023

References

1. Yan, Z., & Xu, Y. (2018). Data-driven load frequency control for stochastic power systems: A deep reinforcement learning method with continuous action search. *IEEE Transactions on Power Systems., 34*, 1653–1656.
2. Fathy, A., & Kassem, A. M. (2019). Antlion optimizer-anfis load frequency control for multi-interconnected plants comprising photovoltaic and wind turbine. *ISA Transactions, 87*, 282–296.
3. Liu, F., Zhang, K., & Zou, R. (2022). EID-based load frequency control for interconnected hybrid power system integrated with RESs. *CSEE Journal of Power and Energy Systems*.
4. Zhang, Z., Dou, C., Yue, D., & Zhang, B. (2021). Predictive voltage hierarchical controller design for islanded microgrids under limited communication. *IEEE Transactions on Circuits and Systems I: Regular Papers., 69*, 933–945.
5. Dreidy, M., Mokhlis, H., & Mekhilef, S. (2017). Inertia response and frequency control techniques for renewable energy sources: A review. *Renewable and Sustainable Energy Reviews., 69*, 144–155.
6. Arya, Y. (2019). Agc of pv-thermal and hydro-thermal power systems using ces and a new multi-stage fpidf-(1+ pi) controller. *Renewable Energy, 134*, 796–806.
7. Guo, J., Zhang, Z., & Dou, C. (2022). Bi-level economic dispatch strategy for electric vehicles connecting to virtual power plant based on information gap decision theory and dynamic time-of-use price. *Electric Power Automation Equipment, 42*, 77–85.
8. Zhang, Z., Dou, C., Yue, D., Zhang, Y., Zhang, B., & Zhang, Z. (2022). Event-triggered hybrid voltage regulation with required bess sizing in high-pv-penetration networks. *IEEE Transactions on Smart Grid, 13*(4), 2614–2626.
9. Dhundhara, S., & Verma, Y. P. (2018). Capacitive energy storage with optimized controller for frequency regulation in realistic multisource deregulated power system. *Energy, 147*, 1108–1128.
10. Khodabakhshian, A., & Edrisi, M. (2008). A new robust pid load frequency controller. *Control Engineering Practice., 16*, 1069–1080.
11. Farivar, F., Bass, O., & Habibi, D. (2022). Decentralized disturbance observer-based sliding mode load frequency control in multiarea interconnected power systems. *IEEE Access., 10*, 92307–92320.
12. Ghoshal, S. (2004). Application of ga/ga-sa based fuzzy automatic generation control of a multi-area thermal generating system. *Electric Power Systems Research., 70*, 115–127.
13. Dahiya, P., Sharma, V., & Sharma, R. (2015). Optimal generation control of interconnected power system including dfig-based wind turbine. *IETE Journal of Research., 61*, 285–299.
14. Gozde, H., Taplamacioglu, M., & Kocaarslan, I. (2012). Comparative performance analysis of artificial bee colony algorithm in automatic generation control for interconnected reheat thermal power system. *International Journal of Electrical Power & Energy Systems., 42*, 167–178.
15. Abdelaziz, A., & Ali, E. S. (2015). Cuckoo search algorithm based load frequency controller design for nonlinear interconnected power system. *International Journal of Electrical Power & Energy Systems., 73*, 632–643.
16. Golpira, H., & Bevrani, H. (2011). Application of ga optimization for automatic generation control design in an interconnected power system. *Energy Conversion and Management., 52*, 2247–2255.
17. Davtalab, S., Tousi, B., & Nazarpour, D. (2022). Optimized intelligent coordinator for load frequency control in a two-area system with pv plant and thermal generator. *IETE Journal of Research, 68*(5), 3876–3886.
18. Dahiya, P., & Saha, A. K. (2022). Frequency regulation of interconnected power system using black widow optimization. *IEEE Access., 10*, 25219–25236.
19. Lu, K., Zhou, W., Zeng, G., & Zheng, Y. (2019). Constrained population extremal optimization-based robust load frequency control of multi-area interconnected power system. *International Journal of Electrical Power & Energy Systems., 105*, 249–271.
20. Chandrakala, K. V., Balamurugan, S., & Sankaranarayanan, K. (2013). Variable structure fuzzy gain scheduling based load frequency controller for multi source multi area hydro thermal system. *International Journal of Electrical Power & Energy Systems., 53*, 375–381.
21. Sudha, K. R., Raju, Y. B., & Sekhar, A. C. (2012). Fuzzy c-means clustering for robust decentralized load frequency control of interconnected power system with generation rate constraint. *International Journal of Electrical Power & Energy Systems, 37*(1), 58–66.
22. Hemeida, A. M. (2005). Wavelet neural network load frequency controller. *Energy Conversion and Management., 46*, 1613–1630.
23. Zribi, M., Al-Rashed, M., & Alrifai, M. (2005). Adaptive decentralized load frequency control of multi-area power systems. *International Journal of Electrical Power & Energy Systems, 27*(8), 575–583.
24. Yang, G., & Qu, Z. (2012). Load frequency control of power systems based on mpc algorithm. *Power System Technology, 36*, 105–110.
25. Dutta, A., & Prakash, S. (2020). Load frequency control of multi-area hybrid power system integrated with renewable energy sources utilizing facts & energy storage system. *Environmental Progress & Sustainable Energy., 39*, e13329.
26. Mi, Y., Fu, Y., Wang, C., & Wang, P. (2013). Decentralized sliding mode load frequency control for multi-area power systems. *IEEE Transactions on Power Systems., 28*, 4301–4309.
27. Zhao, N., Gorbachev, S., Yue, D., Kuzin, V., Dou, C., Zhou, X., & Dai, J. (2022). Model predictive based frequency control of power system incorporating air-conditioning loads with communication delay. *International Journal of Electrical Power & Energy Systems, 138*, 107856.
28. Li, B., & Roche, R. (2020). Optimal scheduling of multiple multi-energy supply microgrids considering future prediction impacts based on model predictive control. *Energy, 197*, 117180.
29. Zhang, Z., Yue, D., Dou, C., & Zhang, H. (2020). Multiagent system-based integrated design of security control and economic dispatch for interconnected microgrid systems. *IEEE Transactions on Systems, Man, and Cybernetics: Systems, 51*, 2101–2112.

30. Zhang, Z., Zhang, Y., Yue, D., Dou, C., Ding, X., & Zhang, H. (2021). Economic-driven hierarchical voltage regulation of incremental distribution networks: A cloud-edge collaboration based perspective. *IEEE Transactions on Industrial Informatics., 18*, 1746–1757.
31. Le Floch, C., Bansal, S., Tomlin, C. J., Moura, S. J., & Zeilinger, M. N. (2017). Plug-and-play model predictive control for load shaping and voltage control in smart grids. *IEEE Transactions on Smart Grid, 10*(3), 2334–2344.
32. Ali, H. H., Kassem, A. M., Al-Dhaifallah, M., & Fathy, A. (2020). Multi-verse optimizer for model predictive load frequency control of hybrid multi-interconnected plants comprising renewable energy. *IEEE Access., 8*, 114623–114642.
33. Esposito, C., Castiglione, A., Pop, F., & Choo, K.-K.R. (2017). Challenges of connecting edge and cloud computing: A security and forensic perspective. *IEEE Cloud Computing., 4*, 13–17.
34. Liu, J., Yao, Q., & Hu, Y. (2019). Model predictive control for load frequency of hybrid power system with wind power and thermal power. *Energy, 172*, 555–565.
35. Hui, H., Ding, Y., Chen, T., Rahman, S., & Song, Y. (2020). Dynamic and stability analysis of the power system with the control loop of inverter air conditioners. *IEEE Transactions on Industrial Electronics., 68*, 2725–2736.
36. Xia, Y., Zhang, Y., Dai, L., Zhan, Y., & Guo, Z. (2022). *A brief survey on recent advances in cloud control systems*. Express Briefs.
37. Elmelegi, A., Mohamed, E. A., Aly, M., Ahmed, E. M., Mohamed, A.-A.A., & Elbaksawi, O. (2021). Optimized tilt fractional order cooperative controllers for preserving frequency stability in renewable energy-based power systems. *IEEE Access, 9*, 8261–8277.
38. F. Wei, "Study on active compensation method for long time delay and data loss of networked control system," *Chongqing University.*, 2017.